Recrystallization Texture and Shear Band Formation in Bending of Metal Material

*Hiroshi Kaneko[*1], Tatsuya Morikawa[*2], Masaki Tanaka[*2], Hirofumi Inoue[*3], Kenji Higashida[*4]*

ABSTRACT The effect of controlling the crystal orientation distribution (= texture) with respect to the bending workability of the metal materials and its mechanism are reported. In this study, at first, the crystal orientation map in the material after bending was analyzed in detail, and it was elucidated that the shear bands concentrate in the planar region at a 35-40° inclination from the surface. Bending cracks occur along this shear bands and are an important control factor for the workability. Next, it was found that by controlling the texture of the workpiece, the development of the shear band is suppressed and the bending workability is remarkably improved. For these mechanisms, the assumption of applying the principle of the minimum plastic work to the multiple slip deformation of the crystal is effective, and the angle of the shear deformation and the crystal orientation in which the shear deformation hardly occurs could be explained consistently.

Furukawa Electric has been engaged in the business in many areas such as infrastructure, automobiles, electronics and others from materials. The new technology, found this time, to control the crystal state of the metallic materials will be further developed in a number of applications, and we will address to various requests from customers on improvement of design freedom, productivity development etc..

1. INTRODUCTION

Shear bands are an area where the shear strain is concentrated through several crystal grains. In the area, the grains deform cooperatively despite the different geometric arrangements of the slip system in each grain. The majority of the macroscopic strain is borne by the shear bands. To the mechanisms of such shear bands, much interest has been submitted. Many researchers have used various approaches to study this mechanism, including microstructural analyses[1)-5)], crystallographic geometric softening[6)-8)], continuum mechanics[9),10)], and the crystal plasticity finite element method (CPFEM)[11)-13)]. Many of these studies have done by employing heavily rolled materials. The formation process of the shear bands depends on material properties such as the ease of occurrence of twinning deformation or the rolling texture[4)].

[*1] Laboratories for Fusion of Core Technologies, R&D Division
[*2] Department of Materials Science and Engineering, Kyushu University
[*3] Department of Materials Science, Graduate School of Engineering, Osaka Prefecture University
[*4] National Institute of Technology, Sasebo College

Shear bands are observed not only during cold-rolling but also during bending. Since the surface is free during bending, shear plastic flow is more likely to occur. During the plastic bending process, cracks are often initiated in the shear bands. It has been reported that bending workability is notably influenced by a recrystallization texture[14)-16)]. There is a need for further investigation to elucidate the mechanism behind the dependence of shear bands on crystallographic orientation. A crystallographic orientation markedly influences several fundamental deformation behavior, including (i) the interaction of dislocations and the manner of dislocation accumulation[17),18)], (ii) the easiness of cross slip[19)] ,and (iii) the sum of crystal shear due to slip deformation, i.e., the Taylor factor[20)-22)]. Usually, these effects are interlaced.

In this study, to focus on the (iii), we employed polycrystalline samples of high-concentration Cu–Ni–Si alloys with various recrystallization textures. The Cu–Ni–Si system is an alloy with high hardness due to δ-Ni$_2$Si precipitation[23)-26)]. To observe in detail the inhomogeneous deformation associated with the change of surface shape, the FE-SEM/EBSD method was used. By these methods, the formation mechanism and the texture dependence of the shear bands during bending were examined.

2. EXPERIMENTAL PROCEDURE

2.1 Sample Preparation and Evaluation on the Bending Workability

After melting and homogenizing the Cu-Ni-Si system alloys, the alloys were hot rolled and milled to remove surface scale. The chemical compositions are shown in Table 1. Then, the 0.2-mm-thick strips were obtained by cold rolling and annealing. Test samples were then prepared by solution treatment and aging. Four kinds of samples with different textures in a 3.8%Ni alloy were prepared by the arrangement of conditions in the above process. Based on the {111}, {100} and {110} pole figures measured on the sample surface[16] by the Schulz reflection method using the CuKα radiation, we analyzed the orientation distribution function (ODF) at the 22nd rank.

Table 1   Chemical composition of samples (mass%).

	Ni	Si	Zn	Sn	Cr	Mg	Cu
2.3Ni alloy [UNS 64775]	2.30	0.65	0.50	0.15	0.15	0.10	Bal.
3.8Ni alloy [UNS 64790] No.1-4	3.76	0.89	0.51	0.15	0.20	0.09	Bal.

Because of recrystallization during the solution treatment, the influence of dislocations prior to bending was able to be ignored. The mean grain size measured with the intercept method including twin boundaries were 3.7 µm, 4.0 µm, 3.8 µm, 3.5 µm, and 4.6 µm for Nos. 1–4 and the 2.3% Ni alloy, respectively. These values were similar to one another, and thus, their influence could be ignored[27]. Because the solution treatment and aging conditions were identical for Nos. 1–4, the precipitation states were also identical. In this way, these Nos. 1-4 allowed for evaluation of only the influence of the recrystallization texture.

The tensile test was performed at room temperature using the specimen of JIS-13B, in which the rolling direction was parallel to the tensile direction and the strain rate was $3.3 \times 10^{-3} \mathrm{s}^{-1}$.

2.2 Shear Band Analysis by FE-SEM/EBSD Method

Bending test, in which the sample was bent into a W-shape, was performed using a press metal die as shown in Figure 1 (a). To change the surface strain due to bending, the bending radius R was changed from 0 mm to 0.4 mm. (These bending conditions are indicated as 0R and 0.4R, respectively, in this paper.) The smaller the bending radius, the larger the strain induced on the surface. The sample coordinate systems are shown in Figure 1 (b): 1 is the longitudinal direction (LD) of bending, 2 is the transversal direction (TD) of bending, and 3 is the normal direction (ND) of the sample surface. The rolling direction in the sample preparation corresponds to the LD. The width and the thickness of the sample were 10 mm and 0.2 mm, respectively. Because the sample width is sufficiently greater than the thickness, contraction in the TD was negligible near the center along the width[28].
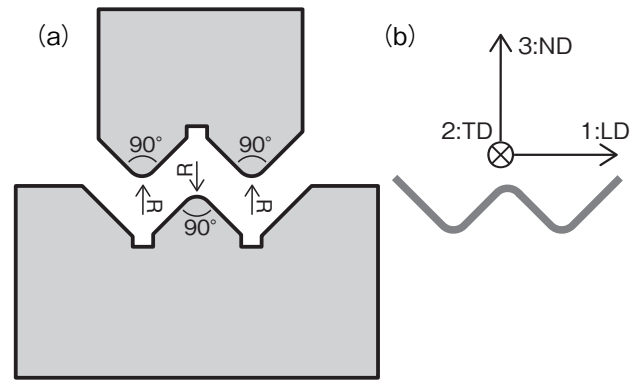
Figure 1   (a) Press metal die used in the 90° W-type bending test and (b) sample coordinate system in the bending sample.

The deformation microstructures and crystallographic orientations in the bent samples were observed using the field emission scanning electron microscopy/electron back-scattering diffraction (FE-SEM/EBSD) method. This observation was performed on the TD cross section at the apex of bending. The cross section was obtained by argon ion irradiation to minimize the influence of the affected layer. The scan step was set to 0.1 µm, and the measurement points with confidential index (CI) values of less than 0.05 were not reliable and were excluded[29]. These points were shown in black on the crystal direction and image quality (IQ) maps. Using the crystal grain boundaries as a marker in the EBSD map, we examined the localized shear deformation. Specifically, we used the grain boundaries that were perpendicular to the shear direction. In addition, based on the distribution of the IQ, we qualitatively identified the strain distribution. The IQ is a measure of the clarity of the Kikuchi pattern, and the more the lattice becomes strained, the more it decreases. However, because the IQ depends on the crystallographic orientation and minor unevenness of the surface, we used this parameter along with the crystal direction map.

The plane strain compression and the two types of shear strains were defined as shown in Figure 2, where positive and negative shear were defined based on the method used by Dillamore, et al.[6]. The angle between the LD and the shear direction was defined as β.

(a) plane strain compression

(b) positive shear strain

(c) negative shear strain

3:ND

2:TD   1:LD
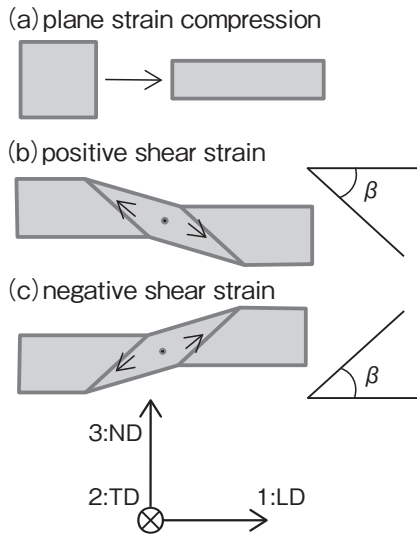
Figure 2 Definition of strain mode in the schematic viewed from the TD: (a) plane strain compression, (b) positive shear strain, and (c)negative shear strain.

3. RESULTS

3.1. Orientation distribution functions (ODFs)

Figure 3 shows the ODF analysis. The Euler angles of typical texture components are displayed at the bottom right of the figures. Figure 3(a) shows the strong development of the Cube orientation {001}<100> and the R orientation {231}<346> in No. 1. Figure 3(c) shows the development of the BR orientation {362}<853> and the RDW (RD-rotated Cube) orientation {012}<100> in No. 3. Figure 3(b) shows that No. 2 has the same texture component as those in No. 1 and No. 3. Figures 3(d) and (e) show that the maximum orientation density was 4, indicating a random texture in No. 4 and the 2.3% Ni alloy. These four kinds of texture components are commonly observed in copper alloys[30]-[32].

Contour Levels: 3 6 9 12 15 18 21 24 27 30 33 36 39 42 45

(a) (b)

(c) (d)

(e)

$\varphi_2=0°$	5°	10°	15°
25°			
20°	30°	35°	
45°			
40°	50°	55°	
60°	65°	70°	75°
		$\rightarrow \varphi_1$	
80°	85°	90°	Φ

○ Cube (001) [100]   ■ Goss (011) [100]   ▲ RDW (012) [100]
◆ WT (122) [221]   ▼ BR (252) [743]   ● R (132) [643]
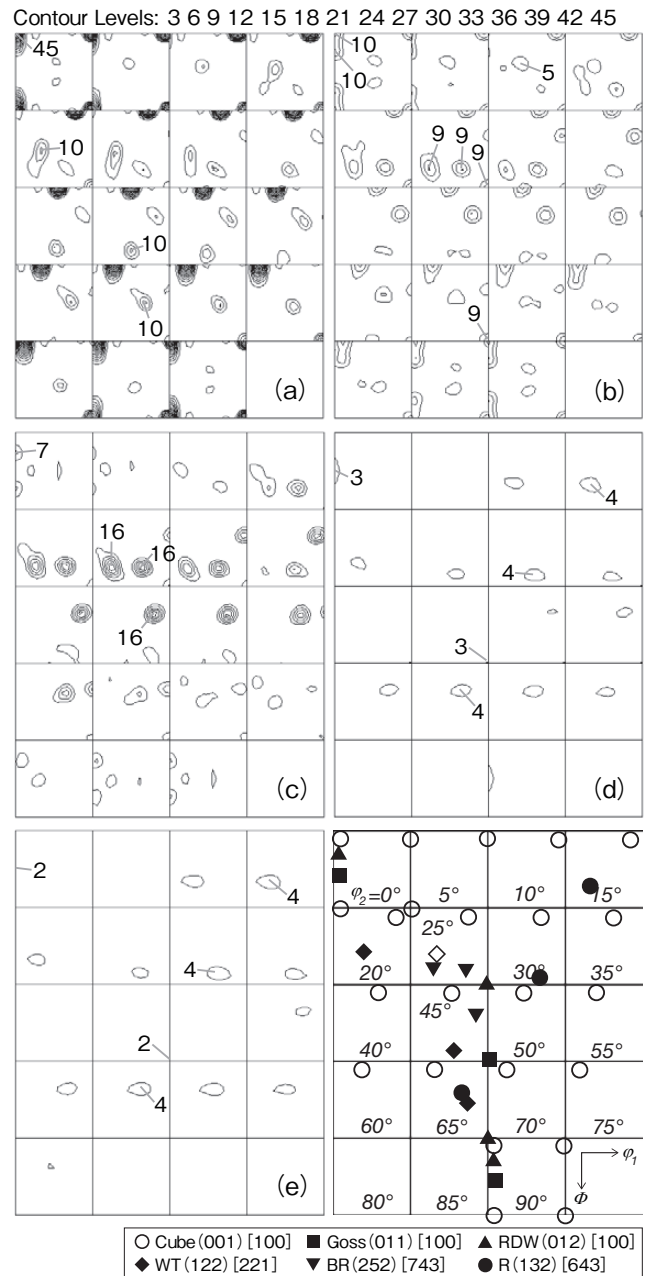
Figure 3 Orientation distribution function (ODF) analysis: (a) No. 1, (b) No. 2, (c) No. 3, (d) No. 4, and (e) the 2.3% Ni-alloy. Euler angles of the typical texture component are displayed at the bottom right of the figures.

3.2. Mechanical tests

Figure 4 shows stress–strain curves. In this figure, a result from ordinary tough pitch copper (TPC) is also displayed for comparison. Although the slope of the elastic region was different[33], the plastic flow stresses for Nos. 1–4 with different textures were nearly the same. Compared to that of the 2.3% Ni alloy, the yield strength of Nos. 1-4 was 100 MPa higher, and the hardening rates of these samples were also higher. Compared to TPC, the yield stress and work hardening rate of the Cu-Ni-Si alloys were very high by the effect of the fine precipitates. The breaking strains were from 0.14-0.15 for all five samples. These were mostly uniform elongation.
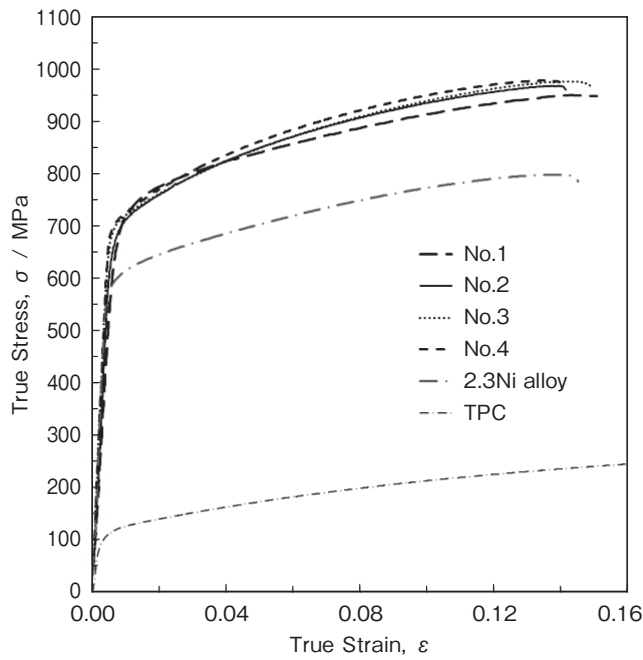
Figure 4 Stress-strain curves from the uniaxial tensile test. Tough-pitch copper (TPC) is shown for comparison.

Table 2 shows the results of observing the bent surface from the ND with the optical microscope. Under 0R and 0.1R conditions, large cracks formed in No. 3 and No. 4, whereas small cracks formed in No. 2 and no crack formed in No. 1. Specifically, No. 1 was found to have better bending workability than the 2.3% Ni alloy with low flow stress. A comprehensive determination based on the scale of the cracks indicated that the order of bending workability was as follows: No. 1 > the 2.3% Ni alloy > No. 2 > No. 4 > No. 3. Specifically, a correlation was observed between the volume of the BR orientation and decreasing bending workability. In this way, the bending workability was notably different depending on the texture and had no correlation with the breaking strain in the tensile test.

Table 2 Bent surface observations. Conditions observed with the FE-SEM/EBSD are underlined.

	0R	0.1R	0.2R	0.3R	0.4R
No.1	good	good	good →EBSD	good	good →EBSD
No.2	crack	crack	good	good	good
No.3	large crack	large crack	large crack	crack	good
No.4	large crack	crack →EBSD	crack	crack	good →EBSD
2.3Ni alloy	crack	good	good	good	good

Figures 5 (a)-(e) show the optical micrographs obtained from the TD section after the 0R bend test of Nos. 1-4 and the 2.3% Ni alloy, respectively. A low magnification micrograph is also displayed at the bottom right of the figures, in which the observed region corresponds to the apex of bending. No. 1 showed a particularly favorable bent outer surface that was slightly wrinkled. In contrast, a large crack was observed in No. 3 and No. 4. In No. 2 and the 2.3% Ni alloy, a small crack was observed. The shapes of the cracks from the surface were linear as indicated by the white arrows in Figs. 5 (b)-(e). The cracks from the surface were not generated along the grain boundaries. They developed in a direction inclined at 35-40° to the upper surface.
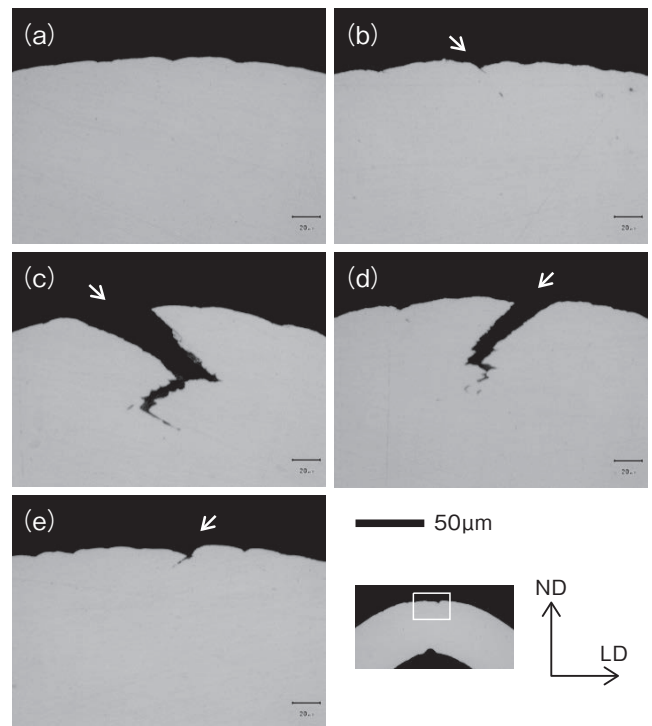
Figure 5 Forms after the 0R bending test on the TD cross section at the central part of the sample's width: (a) No. 1, (b) No. 2, (c) No. 3, (d) No. 4, and (e) the 2.3% Ni alloy. White arrows indicate the cracks.

3.3. EBSD analysis in the randomly oriented sample (No. 4)

The results from No. 4, which had a random texture show how multiple crystal grains deform cooperatively. Figures 6(a)-(c) show the crystal direction map in the LD and TD and an IQ map obtained from No. 4 after the 0.4R bending test, respectively. The sets of arrows and numbers underlined in Figure 6 (b) indicate the shear direction and the shear displacement in micrometers estimated by steps of the grain boundaries, respectively. These steps were confirmed at 16 locations and were 0.3-0.9 µm in length. Among them, a row of the shear displacements was observed from the upper center (indicated by grain A in Figure 6 (b)) to the bottom right (indicated by grain B). Also, due to the local orientation change around the TD, we were able to see the shear strain. In the shear deformation areas in grains A and B, the crystal direction along the LD changed substantially compared to the surroundings: from purple to watery in grain A and form damask to faint yellow in grain B (Figure 6 (a)). Whereas, the crystal directions along the TD were nearly unchanged (Figure 6 (b)). In this way, the shear bands through several grains were confirmed even under the small strain. In addition, the yellow arrows in Figure 6 (c) indicate the surface steps formed by the shear bands, which were demonstrated by a relatively dark band-like contrast in the IQ map. The shear bands were in a direction inclined at 36° to the LD.

Figures 7 (a)-(c) show the crystal direction map in the LD, an IQ map, and an optical micrograph of the same region after the 0.2R bending test, respectively. We were able to see the negative shear band from the curvature of the parallel twin boundary in the *n*-region and the positive shear band from the steps of the grain boundary in the *p*-region as shown in Figure 7 (a). The width of these shear bands was approximately 5 µm. In the *n*-region, there were sets of grains with the same orientations on both sides of the crack. This indicated that the mode-2 crack developed inside the shear band in the *n*-region.
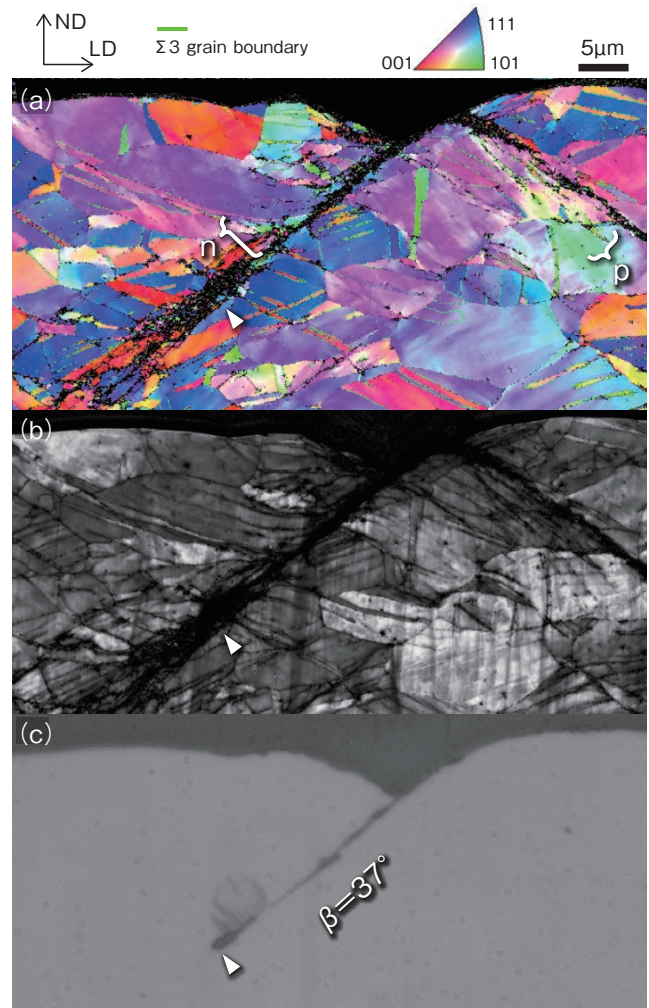
Figure 7 FE-SEM/EBSD images of sample No. 4 after the 0.2R bending test: (a) crystal direction map in the LD, (b) image quality map, and (c) optical microscope image. White triangles indicate the end point of the crack. The 'n' and 'p' in (a) indicate the negative and positive shear bands, respectively.

Figure 6 FE-SEM/EBSD image of sample No. 4 after the 0.4R bending test: (a) crystal direction map in the LD, (b) crystal direction map in the TD, and (c) image quality map. The 'x' in (a) indicates grains A and B. The set of arrows and the underlined numbers in (b) indicate the shear direction and the shear displacement, respectively. The yellow arrows in (c) indicate the surface steps formed by the shear bands.

Figure 8 shows an enlarged image near the crack in Figure 7, demonstrating the state of the sample before the displacement due to shear banding generated the crack. We cropped the image in the upper left of the crack that is surrounded by a dotted yellow line and physically moved it along the crack (along the yellow arrow) so that the grains of the same orientation would meet. Figure 8 shows the formation of an angular groove with a depth of approximately 4 µm just before shear banding generated the crack. This depression was formed by both the negative and positive shear bands and then, acted as a stress concentration point. Thus, this groove triggered concentration of the shear and generation of the crack.

(a)

(b)
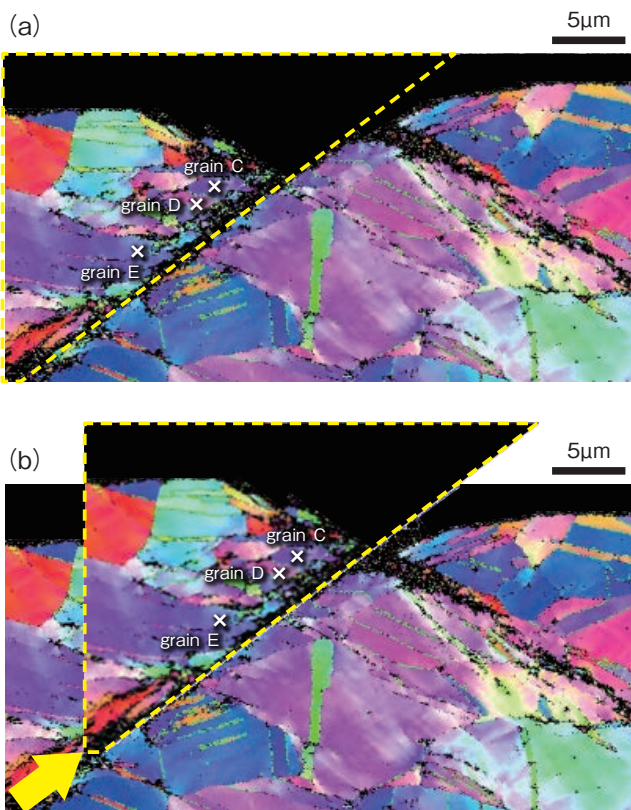
Figure 8　Enlarged image near the crack in Figure7 demonstrating the state before the displacement due to shear banding with generation of the crack. The yellow arrow indicates the vector of parallel moving of the cropped area surrounded by yellow dashed line. The 'x' indicates grains C, D, and E.

In this way, the localized shear deformation and resulting surface shape changes occurred in conjunction. At the locations where cracks were observed, the positive and negative shear bands developed in two directions, which is a typical configuration[11),15)]. The formation process of these shear bands and the crack are schematically illustrated in Figure 9. First, localized shear deformation occurred [i], which induced the steps on the sample surface. The steps caused a stress concentration [ii] and the initiation of new shear deformation [iii]. With the formation of the new shear band, the stress concentration encour-

aged at the groove on the surface [vi], and then, the generation of a mode II crack was induced in the shear band with a large amount of shear displacement [v]. Thus, the shear bands and the surface shape change formed a vicious circle towards the generation of a crack.
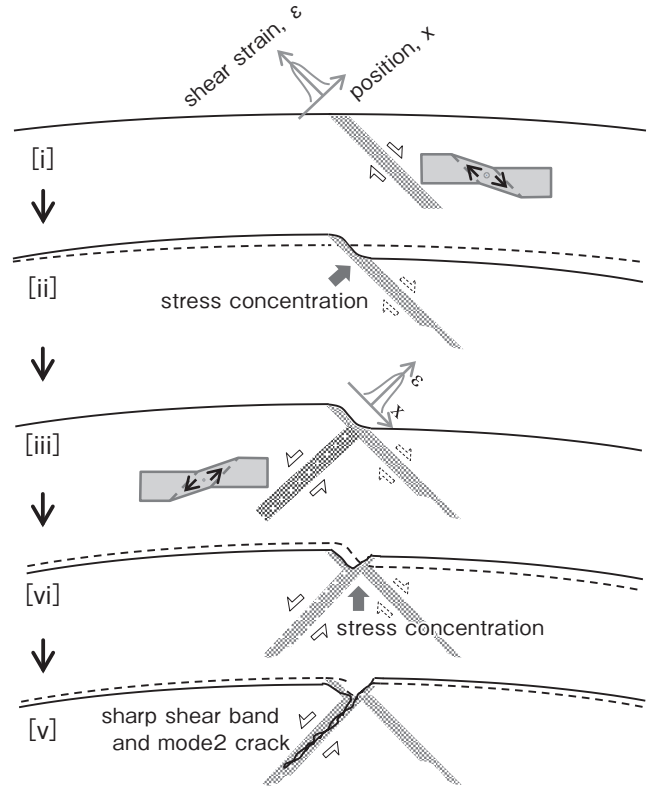
Figure 9　Schematic diagram of the plastic flow and the surface shape change during bending. [i]-[v] present the progress of bending.

3.4.　EBSD analysis in the Cube-orientation developed sample (No. 1)

Figures 10 (a) and (b) show the crystal direction map in the LD and the IQ map of No. 1 after the 0.4R bending test, respectively. The sets of arrows and the numbers underlined in Figure 10 (a) are labeled in the same way as in Figure 6 (b). There were very few shears in this case compared to No. 4. Figures. 11 (a)-(c) show the crystal direction map in the LD and TD and the IQ map after the 0.2R bending test, respectively. The shear bands and surface unevenness were quite minor compared with No. 4. Specifically, in the Cube grains, local shearing was not confirmed. In addition, the shading in the IQ map was dense, indicating uniform deformation. Even if the bending deformation progressed, the crystallographic orientation close to the Cube orientation was maintained, although there was dispersion around the TD.
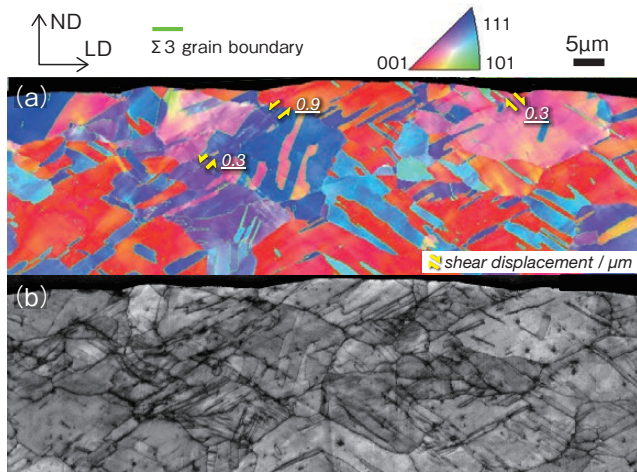
Figure 10 FE-SEM/EBSD images of sample No. 1 after the 0.4R bending test: (a) crystal direction map in LD and (b) image quality map. The set of arrows and the underlined numbers in (a) indicate the shear direction and shear displacement, respectively.
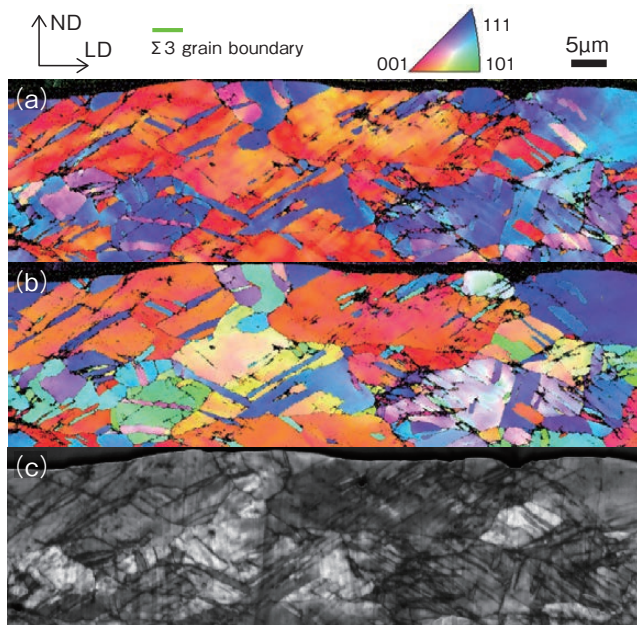
Figure 11 FE-SEM/EBSD observation of sample No. 1 after the 0.2R bending test: (a) crystal direction map in the LD, (b) crystal direction map in the TD, and (c) image quality map.

4. DISCUSSION

4.1 Consideration based on Taylor's Theory Assuming Both Strain Modes on the Plane Strain Compression and the Shear Strain

It was experimentally revealed in this study that bending workability was related to inhomogeneous microstructures such as shear bands, which were significantly influenced by the sample's preferred crystallographic orientation distribution. To examine the formation conditions of the shear bands, we will discuss the Taylor factor M as a criterion of the change in deformation modes. The velocity gradient tensor L is as follows:

$$L^{pla} = d\dot{\varepsilon}\begin{pmatrix} 1 & 0 & 0 \\ 0 & 0 & 0 \\ 0 & 0 & -1 \end{pmatrix} \quad for\ plane \qquad (1)$$

$$L^{shear-posi} = d\dot{\varepsilon}\begin{pmatrix} 1 & 0 & -\tan\beta \\ 0 & 0 & 0 \\ \cot\beta & 0 & -1 \end{pmatrix} \quad for\ positive\ shear \quad (2)$$

and

$$L^{shear-nega} = d\dot{\varepsilon}\begin{pmatrix} 1 & 0 & \tan\beta \\ 0 & 0 & 0 \\ -\cot\beta & 0 & -1 \end{pmatrix} \quad for\ negative\ shear \quad (3)$$

where $d\dot{\varepsilon}$ is a scalar measure of the strain rate. The strain velocity D in L is the combination of multiple {111}<110> slip deformations.

$$D = \sum_i \dot{\gamma}^{(i)}\left[\frac{1}{2}\left(s^{(i)} \otimes m^{(i)} + m^{(i)} \otimes s^{(i)}\right)\right] \qquad (4)$$

where $\dot{\gamma}^{(i)}$ is the slip rate, m is the slip plane normal vector, s is the slip direction vector, and i is the number of the slip system. Based on the full constraint (FC) model, five or more slip systems are active. Among the combinations of the slips that satisfy the equation (4), we selected the one with the minimum sum of slip shear as the Taylor factor[20].

$$M = min\left(\sum_i \left|d\dot{\gamma}^{(i)}\right|\right) / d\dot{\varepsilon} \qquad (5)$$

Then, the flow stress σ is expressed in terms of the critical resolved shear stress of the slip system τ.

$$\sigma = M \cdot \tau \qquad (6)$$

Because it was thought that the influence of the crystallographic orientation on τ should be small enough to be ignored in the Cu-Ni-Si alloys, we considered the influence of M on the flow stress and the plastic work.

First, we derived M^{pla} from L^{pla} and M^{shear} from L^{shear} for some grains in the randomly oriented sample (No. 4). Figure 12 shows the M^{pla} and M^{shear} of grains A and B shown in Figure 6 and grains C, D, and E shown in Figure 8 as a function of the shear angle β. The values of M^{pla} are indicated by dashed lines in the figures. We substituted the crystallographic orientations at the point near the shear bands indicated with an 'x' in Figure 6 (a) and Figure 8 for the crystallographic orientations at the time that the shear deformation had started. As shown in Figure 12 (a), grains A and B had a very different M^{pla} and M^{shear} depending on the different crystallographic orientation. On the other hand, both grains had a common range of β where M^{shear} was lower than M^{pla} for β=30-40°. This indicated that the shear deformation along 30-40° was

relatively likely to occur. M^{shear} for β=32-36° was particularly low. The result of this calculation corresponded well with the observation that the shear band penetrated both grains with β=36° (Figure 6). A similar tendency was shown in Figure 12 (b), in which the shear deformation was relatively likely to occur with a range of β=31-44° in grain C and β=33-44° in grain D and E. A particularly low common angle was 36°, which corresponded well with a shear band and crack penetrating these grains at 37° (Figure 7). Even if the texture was random, there was a commonly advantageous deformation mode in neighboring grains, which induced the generation of a shear band penetrating these grains.
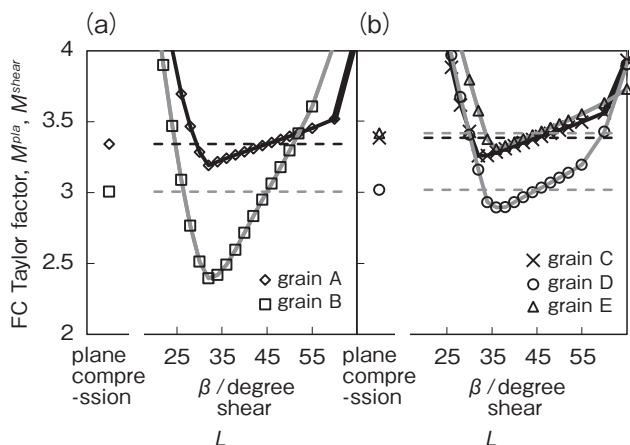
Figure 12 Relationship between the FC (full constraint) Taylor factor and strain mode: (a) grains A and B and (b) grain C, D, and E. Dashed lines indicate the values of M^{pla}.

Second, assuming that the orientation distribution did not change significantly as the bending progressed, M^{plane} and M^{shear} were calculated regarding typical recrystallization orientations. With regard to the orientation near the Cube and the RDW orientations, $M^{pla} \fallingdotseq M^{shear}_{min} \fallingdotseq 2.5$. This indicated that a shear was not favorable, which was the reason that No. 1 did not form shear bands easily and the reason for the good bending workability of No. 1 and No. 2. On the other hand, for the BR orientation, where a correlation with lowering bending workability was observed, M^{pla}=3.8 and M^{shear}_{min}=3.3. This indicated that the shear mode was advantageous in this case. This was likely the reason for the largest cracks in No. 3. For the R orientation, M^{pla}=3.5 and M^{shear}_{min}=3.4. These results were intermediate when selecting a deformation mode.

Last, we calculated the average Taylor factor $\overline{M^{pla}}$ using the ODF analysis coefficients[16], which were 3.08, 3.22, 3.33, and 3.29 for Nos. 1–4, respectively. A small $\overline{M^{pla}}$ correlated with a good bending workability. Since M^{pla} was relatively low for the M^{shear}, the shear band was further prevented. In this way, we were able to interpret the series of experimental results with the FC Taylor theory assuming L^{pla} and L^{shear}.

4.2 Future Issues for the Microstructure Change During the Bending and for the Factors Affecting the Flow Stress

In the above discussion, we assumed that the strain velocity tensor D was only composed of the crystal slip deformation. On the other hand, orientation gradients were clearly observed in the deformed grains with EBSD analysis. This suggested that a part of D was compensated for by the geometrically necessary dislocations (GNDs). The GNDs should increase the flow stress through curvature and twisting of the lattice[34] while also corresponding to a decrease in the sum of the slip shear strains than that of full constraint condition[35]. At present, however, the clear dependence of crystallographic orientation on the density of the GNDs has not been confirmed. More strictly, examination of this influence is necessary. In addition, in the shear band, it is possible to change τ in Equation (6) if a dynamic recovery or morphological change of precipitate were to occur. The influences of the deformation microstructure on slip resistance should be included in any future macroscopic deformation analyses.

5. CONCLUSION

Inhomogeneous deformation in the bending for the high-concentration Cu–Ni–Si alloys with various recrystallization textures was examined.

1) In the sample with a random texture, shear banding was observed even under a small strain. The shear bands caused a change in the surface shape, at which point, a crack was initiated. The crack propagated in the shear bands.

2) In the sample with a strongly developed Cube orientation, the shear bands and the accompanying surface roughness were notably suppressed. Compared to the 2.3% Ni alloy with a random orientation, the bending workability was better and the strength was ≥20% higher. As such, texture control was shown to be a useful technique that could achieve both a high strength and excellent bending workability.

3) The dependence of crystallographic orientation on the formation of the shear band was discussed using the full constraint Taylor model based on the premise of both the plane strain compression and shear strain modes. Even if the texture was random, there was a common favorable shear mode in neighboring grains, which induced a shear band. The Cube and the RDW orientations were advantageous for suppression of the shear, whereas the BR orientation was not.

REFERENCIES

1) T. Noda: Bull. Jpn. Inst. Met. ,19 (1980). 638-644.
2) K. Morii, H. Mecking, Y. Nakayama: Acta Metall., 33 (1985), 379-386.
3) T. Morikawa, D. Senba, K. Higashida and R. Onodera: Mater. Trans. JIM, 40 (1999), 891–894.
4) K. Higashida and T. Morikawa: Tetsu-to-Hagané, 94 (2008), 576–581.
5) T. Morikawa and K. Higashida: Mater. Trans., 51 (2010), 620-624.
6) I. L. Dillamore, J. G. Roberts and A. C. Bush: Metal Sci., 13 (1979), 73-77.
7) P. Van Houtte, J. Gil Sevillano and E. Aernoudt: Z. Metallk., 70 (1979) 426-432, 503-508.
8) G. R. Canova, U. F. Kocks and M. G. Stout: Scripta Metall., 18 (1984), 437-442.
9) R. Hill and J. W. Hutchinson: J. Mech. Phys. Solids, 23 (1975), 239-264.
10) R. J. Asaro: Acta Metall., 27 (1979), 445-453.
11) M. Dao, M. Li: Phil. Mag. A, 81 (2001), 1997-2020.
12) M. Kuroda, V. Tvergaard: Int. J. Plast., 23 (2007), 244-272.
13) S. Ikawa, M. Asano, M. Kuroda and K. Yoshida: Mat. Sci. Eng. A, 528 (2011), 4050-4054.
14) H. Takeda, A. Hibino and K. Takata: Mater. Trans., 51 (2010), 614-619.
15) H. Kaneko and T. Eguchi: Mater. Trans., 53 (2012), 1847-1851.
16) H. Inoue: Mater. Trans., 56 (2015), 61-69.
17) P. Franciosi, M. Berveiller and A. Zaoui: Acta Metall., 28 (1980), 273-283.
18) T. Ohashi: Phil. Mag. A, 70 (1994), 793- 803.
19) J. Takamura: Bull. Jpn. Inst. Met., 12 (1973), 505-521.
20) G. I. Taylor: J. Inst. Metals, 62 (1938), 307-324.
21) G. Y. Chin, E. A. Nesbitt and A. J. Williams: Acta Metall., 14 (1966), 467-476.
22) W. F. Hossford: Acta Metall, 14 (1966), 1085-1094.
23) M. G. Corson: Rev. Met., 27 (1930), 83-101.
24) S. A. Lockyer and F. W. Noble: L. Mat. Sci., 29 (1994), 218-226.
25) H. Fujiwara, T. Sato and A. Kamio: J. Japan Inst. Metals, 62 (1998), 301-309.
26) T. Hu, J. H. Chen, J. Z. Liu, Z. R. Liu and C. L. Wu: Acta Mater., 61 (2013), 1210-1219.
27) H. Kaneko, K. Hirose, T. Eguchi and N. Tanaka: J. JRICu, 46 (2007), 61-65.
28) H. Kaneko, K. Hirose, K. Sato, N. Tanaka, H. Kanamori, K. Mihara and T. Eguchi: Furukawa Review, 38 (2010), 1-7.
29) D. P. Field: Ultramicroscopy, 67 (1997), 1-9.
30) J. Pospiech and K. Lucke: Z. Metall., 70 (1979), 567-572.
31) K. Ito : J. Japan Inst. Light Metals, 43 (1993), 285-293.
32) O. Engler: Acta Mater., 49 (2001), 1237-1247.
33) H. Kaneko, T. Eguchi and H. Inoue: J. Japan Inst. Met. Mater., 77 (2013), 353-360.
34) K. Higashida, J. Takamura and N. Narita: Mat. Sci. Eng., 81 (1986), 239-258.
35) U. F. Kocks and H. Chandra: Acta Metall., 30 (1982), 695-709.